RSC Advances

ROYAL SOCIETY OF CHEMISTRY

www.rsc.org/advances

$BiOCl/SnS_2$ hollow spheres for the photocatalytic degradation of waste water

Hui Meng[a*], Tingting Wang[a], Xiang Yu[b,c], Yi Zhu[b], Yuanming Zhang[b*]

a. Department of Physics and Siyuan Laboratory, Guangzhou Key Laboratory of Vacuum Coating Technologies and New Energy Materials, College of Science and Engineering, Jinan University, Guangzhou 510632, PR China

b. Department of Chemistry, Jinan University, Guangzhou 510632, PR China

c. Analytical & Testing Center, Jinan University, Guangzhou, 510632, PR China

Abstract

The doping effect of a new dopant to BiOCl as photocatalyst is studied. SnS_2 as a narrow-band-gap semiconductor is used to tune the electronic and band structure of wide-band-gap BiOCl. $BiOCl/SnS_2$ hollow spheres are synthesized by a facile and economic one-pot hydrothermal method. The shell of the hollow shperes is composed by BiOCl and SnS_2, but the outermost layer is BiOCl. $BiOCl/SnS_2$ hollow spheres exhibits much higher photocatalytic activity than pure SnS_2 and BiOCl in the degradation of Rhodamine-B under visible light and sun-light irradiation. The improvement is explained by the band structure tuning effect by SnS_2 and the morphological benefits of the hollow sphere structure.

Keywords:

Halogen bismuth oxide; Tin disulfide; Hollow spheres; Photocatalysis

*: co-corresponding author

Email: tmh@jnu.edu.cn (Hui Meng) ; tzhangym@jnu.edu.cn (Yuanming Zhang)

1. Introduction

Photocatalysis is a hot topic in solar energy conversion and photo-oxidation of organic pollutants.[1-6] A contradiction exists for photocatalyts: wide-band-gap semiconductors usually have high photocatalytic performance but poor response to visible light, which leads to low utilization efficiencies of full solar energy.[7-9]

Band-structure engineering is expected to tune the electronic and band structures of wide-band-gap semiconductors to extend the photo response from the ultra-violet (UV) region to the visible light region.[2, 10-13] Bismuth oxychloride (BiOCl), a layered wide-band-gap ternary semiconductor, has recently attracted considerable attention in photocatalysis.[14-16] BiOCl is an ideal parent semiconductor to be doped by other semiconductors.[17, 18] Doped BiOCl has advantages such as high reduction potential of the holes, low electron-hole recombination rates and the easy formation of oxygen vacancies.[17, 19] Doping is an effective way for band-structure tuning, for example anion such as Iodine doping is reported to broaden the light response range.[10, 19, 20] SnS_2 is a kind of n-type semiconductor with band gap of 2.18-2.44eV, the electronic property and band potentials matches well with BiOCl, in this work SnS_2 is chosen as the dopant to BiOCl to achieve high visible-light-responsive ability.[21-23] Both the valence band and conduction band potentials of SnS_2 are more negative than those of BiOCl, this thermodynamically allows the photogenerated electron transfer from the conduction band of SnS_2 to the conduction band of BiOCl under visible light irradiation, which can enhance the separation of photogenerated electrons and holes in SnS_2 and increase sensitivity of BiOCl.[24-26] Thus, the SnS_2-incorporated BiOCl composites are expected to perform higher visible-light-driven photocatalytic activity than individual SnS_2 and BiOCl.

The burgeoning nanotechnology also sheds light to the possibility of tuning the band structure by constructing superstructures which can make use of the advantage of the wide-band-gap semiconductors and reduce the shortcomings of doping materials.[22-26] BiOCl compounds usually exist in tetragonal matlockite structure, which consists of $[Bi_2O_2]^{2+}$ layers sandwiched between two sheets of Cl^- ions.[15, 16, 18, 19]Therefore, it is difficult to control the morphologies of BiOCl crystals. In most reports BiOCl are layered sheets in micrometer scale.[27, 28] The property of nano-material is greatly influenced by morphology, and shape control becomes vital in the preparation of nano-sized functional materials. Here for the first time we constructed a totally new BiOCl-based nanostructure: hollow spheres with BiOCl at the outmost surface. The

hierarchical architecture can allow multiple reflections of light, which enhances light-harvesting efficiency and thus increase the quantity of photogenerated electrons and holes available to participate in the photcatalytic reaction. [29, 30]

In this work, a general and facile one-pot hydrothermal synthesis of a novel BiOCl/SnS_2 hollow spheres is proposed. The resulted composites show enhanced light harvesting ability and high performance in the degradation of organic pollutants under visible light and sun-light irradiation.

2. Experimental

All the reagents were purchased from Aladdin reagent (China) Co., Ltd and were used as received without further purification. All water was deionized water prepared in lab.

2.1 Synthesis

Synthesis of hexagonal SnS_2 nanoflakes

In a typical preparation process, 1 mmol $SnCl_4 \cdot 5H_2O$, 4.0 mmol Thiourea and 0.2 g Polyvinyl pyrrolidone (PVP) were dissolved in 40mL deionized water. The mixture was vigorously stirred for 30 minutes to ensure homogeneous dispersion. The solution was transferred to a 50mL Teflon-lined stainless steel autoclave and maintained at 120□ for 12h. After cooling to room temperature the product was collected by centrifugation, followed by washing thoroughly with deionized water and absolute ethanol. The final product was dried at 60□ in vacuum for 8h.

Synthesis of BiOCl nanoflakes

The procedures are the same with the synthesis of SnS_2 nanoflakes except the reactant changed into 1 mmol $Bi(NO_3)_3 \cdot 5H_2O$ and 1 mmol KCl dissolved in 40 ml deionized water.

Synthesis of SnS_2-incorporated BiOCl hollow microspheres

The same procedures are applied, the reactant changed into the mixture of 1 mmol $SnCl_4 \cdot 5H_2O$, 4.0 mmol Thiourea, 1 mmol $Bi(NO_3)_3 \cdot 5H_2O$, 1 mmol KCl, 1 mmol citric acid and 0.2 g PVP.

To study the role of PVP and citric acid, parallel experiments are performed without citric acid.

2.2 Physical characterizations

The morphologies of the samples were characterized by field emission scanning electron microscope (FESEM) (JEOL JSM-T300, operated at 10kV) and field emission transmission electron microscope (FETEM) (JEOL SM-6330F, operated 200

kV). Energy dispersive X-ray spectroscopy (EDX) (JEOL JSM-6330F equipped with an X-ray energy dispersive spectrometer) was used to analyze the element composition. The crystal structure of the samples were determined on an X-ray diffractometer (XRD) (MSALXD-2 with Cu-Kα radiation, D/Max-IIIA, Rigaku Co., Japan, CuK1, λ=1.54056 Å) and selected area electron diffraction (SAED). X-ray photoelectron spectroscopy (XPS) spectra were acquired using an ESCA Lab 250 (Thermo VG) with 200 W Al Kα radiation in twin anode and the distance between X-ray gun and sample is about 1 cm. The analysis chamber pressure is about 2×10^{-7} Pa and the pass energy is 20 eV for high resolution scans.

2.3. Photocatalytic performance characterizations

Photocatalytic activities of the samples were evaluated by photo-bleaching of Rhodamine B (RhB) under UV-vis (385-740 nm) and visible light (λ>420 nm) irradiations. Experiments were carried out in a 250 mL cylindrical-shaped-glass reactor at room temperature in the air and at neutral pH conditions. A suspension of 10 mg photocatalyst and 100 ml aqueous solution of RhB (10 mg L^{-1}) was magnetically stirred for at least 2 hours before irradiation to estabilish an adsorption-desorption equilibrium. The optical system used for the photocatalytic reaction consisted of a Xenon lamp (XQ350W) and a 420 nm cutoff filter, which was placed under the reaction cell to completely remove all incoming light with wavelengths shorter than 420 nm to ensure irradiation with visible light only. At specific time intervals, 4 ml suspension were sampled and centrifugated at 5000 rpm for 10 min to remove the photocatalyst powder. The concentration of remnant RhB in the solution after irradiation was analyzed by UV-vis spectrophotometer by recording the variations of the absorbance band maximum at λ=554 nm (RhB).

2.4 Photoelectrochemical Measurements

In the fabrication of the photo anode, 20 mg as-prepared photocatalyst powder and 2 ml ethanol solution were mixed homogeneously. The mixture was sprayed on an FTO (fluorine doped tin oxide) glass and allowed to dry under ambient conditions. Photocurrent was measured by an electrochemical workstation(SP-150 from Bio-Logic Science Instruments) in a standard three-electrode system with the as-prepared samples as the working electrodes with an active area of ca. 6 cm^2, a Pt wire as the counter electrode, and a saturated calomel electrode (SCE) as reference electrode. A 350 W Xe lamp equipped with an ultraviolet cutoff filter (λ>420 nm) was utilized as the visible-light source. A 0.1 M Na_2SO_4 aqueous solution was used as the

electrolyte.

3. Results and discussion

3.1 Characterization of the separately prepared samples

FESEM images (Fig. S1a and b) clearly show that SnS_2 are hexagon nanoflakes with a uniform size of 200~300 nm in length and ~20 nm in thickness. PVP plays an important role in the shape control. As capping agent PVP has long alkyl chains with a molecular weight of 55,000 and the carbonyl groups in the backbone structure determine the shape of SnS_2 by the effect of the Van der Waals force and hydrogen bond. Trace amount of PVP can be selectively adsorbed on certain facets, promoting overgrowth in the specific energetically favorable direction. The microstructure was further characterized by HRTEM. As shown in Fig. S1c and d, the same morphology of hexagon nanoflake was observed which is in good accordance with the FESEM images. The atomic arrangement was observed by HRTEM of a selected part of a single nanoflake shown in Fig. S1d. Clear lattice planes with high crystallinity were observed. The resolved lattice fringe is 0.316 nm and corresponds to the d-spacing of (100) lattice planes of hexagonal phase SnS_2. The SAED inset in Fig.S1d shows hexagonal array of spots, which revealed single crystal structure of the nanoflake. From SAED it is concluded that the [001] orientation is the preponderant growth direction of the SnS_2 nanoflake, which is parallel to the (100) facet.

In this work BiOCl is prepared by a simple hydrothermal reaction of the mixture of $Bi(NO_3)_3 \cdot 5H_2O$ and KCl. Since no morphology control is applied, the morphology of as-prepared BiOCl nanoflakes was asymmetric polygon nanoflakes with a diameter of about 0.4~4μm as shown in the FESEM and FETEM images of Fig. S2. The clear lattice stripe of SAED (inset in Fig.S2c) exhibits the single crystalline nature of the nanoflakes. The diffraction spots of the typical tetragonal phase could be indexed to (110) and (200) facets. The interplanar distance of the lattice is 0.274 nm, which is consistent with the (110) planes of the tetragonal system of BiOCl. The HRTEM in Fig.S2d also confirms that the growth direction of BiOCl flake is along the [001] orientation, which is parallel to the (110) plane.

3.2 Physical characterization of the BiOCl/SnS_2 hollow spheres

From above results it is found that when SnS_2 or BiOCl are prepared separately both are flakes. The difference is SnS_2 are hexagon nanoflakes with smaller size while BiOCl flakes are bigger and have irregular shape. The idea of this work is to extend the light absorption edge of BiOCl to the visible light region by forming BiOCl/SnS_2

composites. It is found citric acid plays a crucial role in the morphology development of the BiOCl/SnS_2 composites. As shown in Fig. 1a and 1b, when no citric acid added the morphology of as-prepared BiOCl/SnS_2 composites is a flower like architecture which is composed by layers of flakes. The flakes have irregular shapes with a thickness of about 50 nm and a width of about 0.5-1.0μm and the shapes are different from either SnS_2 or BiOCl. In the presence of citric acid, the FESEM image (Fig. 1c) demonstrates that the as-obtained product is consisted of monodipersed hollow spheres with a good uniformity and narrow size distribution. The spheres have an average diameter of 500-600 nm and have a hole on the surface, showing hollow structure inside. A magnified image of the hollow spheres (Fig. 1d) exhibits detailed surface information. The shell was composed by nanosheets with a thickness of about 15nm as building unit, the nanosheets form a porous and loose packed surface. At the same time some broken spheres can be found, also proving the hollow structure.

XRD is used to confirm the composition of the BiOCl/SnS_2 composites. Fig.2 shows the XRD patterns of as-synthesized pure SnS_2, pure BiOCl and SnS_2-incorporated BiOCl composites. From Fig.2a and b hexagonal SnS_2 phase and tetragonal BiOCl phase are identified from standard card JCPDS 89-2028 and JCPDS 82-0485, respectively. Both flower-like and hollow spheres of BiOCl/SnS_2 composites are composed by tetragonal BiOCl phase and hexagonal SnS_2 phase, which is proved by the coexistence of all characteristic peaks of SnS_2 and BiOCl phases (Fig. 2c and d). Comparing Fig.2c and d, it is found the full width at half maximum (FHWM) of the XRD peaks in Fig.2d is much wider than that of Fig.2c. According to calculation with Scherrer equation[31] the crystal size of hollow spheres of BiOCl/SnS_2 composites is smaller than the flower-like structure. It is also interesting to note that the ratio between BiOCl (001) peak and SnS_2 (001) peak is different for BiOCl/SnS_2 hollow spheres and flower-like structure, showing difference in crystalline growth. Energy dispersion spectrum (EDS, Fig.S3) also proves the coexistence of Sn, S, Bi, O and Cl elements and the atomic ratio of the elements is in good accordance with the stoichiometric ratio of BiOCl and SnS_2.

Compared with the flower-like structure, the hollow spheres of BiOCl/SnS_2 composites have the advantages of smaller particle size revealed by SEM in Fig.1 and smaller crystal size revealed by XRD in Fig.2. The BiOCl/SnS_2 is expected to have better performance in application of photocatalysis. The questions of how BiOCl and SnS_2 form the hollow spheres, which is on the surface and the details of the structure

of the spheres must be answered before studying the photocatalytic property. Fig.3a and b are TEM images of the BiOCl/SnS_2 spheres. The size and morphology of the sphere are in accordance with the SEM images in Fig.1. Fig.3b is an enlarged picture of the spheres, from which it is observed that the inner part of the sphere is grayer than the shell, proving the hollow structure. On the spheres in the middle of Fig.3a (circled by red ring) some bright parts in the gray area are found, which corresponds to the holes found on the surface of the sphere in Fig. 1c and d. The thickness of the shell of the hollow spheres is found to be about 80 nm from Fig.3b. Fig.3b also shows the spheres are composed by layered nanosheet units connected to each other. The crystal property of the shell of the spheres is studied by HRTEM as shown in Fig.3c. Two d values of lattice spacing are indexed to be 0.215 and 0.343 nm, corresponding to the spacing of the (102) crystal plane of SnS_2 and (101) crystal plane of BiOCl, respectively. This indicates the presence of the mixed phase of SnS_2 and BiOCl in the hierarchical hollow spheres, which is in consistent with XRD results, the (102) peak of SnS_2 and (101) peak BiOCl are presented in the XRD of Fig.2. The SAED pattern (Fig. 3d) indexed out the diffraction patterns of (110) and (101) plane for BiOCl. The (110) plane is parallel to the growth direction of BiOCl and the (101) plane is also observed in the HRTEM in Fig.3c. For SnS_2 only (102) and (011) facet are indexed, (100) facet information is missing. The diffraction rings from the (110) Bragg reflections of tetragonal BiOCl overlaps with the diffraction spots from the (011) Bragg reflections of the hexagonal SnS_2 due to the coincidence of lattice spacing of the two crystals.

In TEM characterization, long time bombardment of the sample surface by high energy electron beam will melt the selected area and make it grow bigger.[32, 33] Based on this observation we randomly selected a flake on the surface of the hollow sphere as labeled by the red ring in Fig.4. After 60s of high energy electron beam bombardment the flake grow bigger (inside the red ring in Fig.4). HRTEM image in Fig.4 shows uniform crystal property of the onsite-grown crystal, the d distance of 0.343 nm corresponds to the (101) facet of BiOCl. This result proves the surface of the hollow sphere is BiOCl. From TEM results a conclusion could be reached: the shell of the hollow sphere is composed by both BiOCl and SnS_2, but the outer most is BiOCl.

To gain detailed information about the dispersion of SnS_2 and BiOCl throughout the whole sphere, Energy dispersive X-ray spectroscopy (EDS) mapping were conducted.

EDS mapping of a typical hollow sphere shows the distribution of the Bi, O, Cl, Sn and S elements (Fig. 5). It is noted that Bi, O, Cl, Sn and S elements are uniformly distributed throughout the sphere. EDS mapping can only show the distribution of the elements, the chemical state and the structure of the sphere still need further characterizations.

The X-ray photoelectron spectroscopy (XPS) is a powerful tool to get information of the chemical state and valence band states of the elements on the surface of the materials. In this work, XPS results can also provide useful information on the structure of the material. XPS spectrum in Fig.6a disclosed the presence of Bi, O, Cl, Sn and S components, as well as C. The result is in accordance with the XRD and EDS results. Typical high-resolution XPS spectra for Bi 4f and Sn 3d are shown in Fig. 6b and 6e. It is clear that the binding energies of Bi $4f_{7/2}$ (159.6 eV) and Bi $4f_{5/2}$ (164.9 eV) in SnS_2/BiOCl composites are higher than those of pure BiOCl (159.1 eV and 164.4 eV), which is characteristic of Bi^{3+}.[18, 25, 27] Nevertheless, the binding energies of Sn $3d_{5/2}$ and Sn $3d_{3/2}$ peaks of SnS_2/BiOCl are located at 486.2 eV and 494.9 eV which lower than those of pure SnS_2 (486.8 eV and 495.3 eV). This is explained by the fact that the Fermi levels of SnS_2 are lower than that of BiOCl, so that the electrons on Bi atom can transfer to the Sn atom in SnS_2 dispersed on the surface of BiOCl, which causes the change in the outer electron cloud density of Bi and Sn ions and makes the Bi $4f_{7/2}$ and Bi $4f_{5/2}$ binding energies increase and Sn $3d_{5/2}$and Sn $3d_{3/2}$ binding energies decrease. The interaction of the Fermi level electron and electron cloud may change the property of individual BiOCl and SnS_2, leading to new properties. Fig. 6c shows the high-resolution XPS spectrum of O 1s, which can be fitted into two peaks. The main peak at 530.7 eV belongs to the Bi-O bonds in $(BiO)_2^{2+}$ an BiOCl, and the peak at 532.1 eV is assigned to the hydroxyl groups on the surface.[27] In the high-resolution spectra of the Cl 2p (Fig. 6d), two peaks at 197.9 and 199.4 eV are attributed to Cl $2p_{3/2}$ and Cl $2p_{1/2}$ respectively, they can be ascribed to Cl^- in BiOCl and SnS_2-incoporated BiOCl composites.[27] Two peaks at 161.5 eV and 162.7 eV shown in Fig. 6f are attributed to S $2p_{3/2}$ and S $2p_{1/2}$, which are characteristic of S^{2-} in SnS_2.[25] In conclusion, according to the XPS results, the coexistence of SnS_2 and BiOCl in the composites is confirmed and the Fermi level electron and electron cloud interact with each other.

3.3 Discussion on the growth mechanism and structure details of the hollow spheres

From TEM of Fig.3b the SnS_2-incorporated BiOCl composite is composed by hollow

spheres. EDS mapping results of Fig.5 proves the distribution of the elements is uniform throughout the spheres. But how SnS_2 and BiOCl form the spheres is not clear. High-angle angular dark field scanning transmission electron microscopy (HAADF-STEM) and bright field scanning transmission electron microscopy (BF-STEM) are used to further verify the structure of the spheres. The BF-STEM images (Fig. S4a and b) are similar to TEM images in Fig.3. However in the HAADF-STEM images (Fig. S4c and d) the outer wall of the hollow spheres has a strong brightness contrast compared with the low brightness contrast of the inner part of the sphere. In the HAADF mode the high brightness contrast shows the presence of heavier elements such as Bi and the low brightness contrast shows the presence of light elements such as Sn. This is a strong proof of the structure of the hollow spheres: BiOCl is in the outer layer and SnS_2 in the inner layer, both of them form the shell of the hollow spheres. This structure is also proved by the high energy electron beam bombardment of the sample as discussed in Fig.4. XPS results also support this conclusion. From Fig.6e and f it is noted that on the surface of the SnS_2-incorporated BiOCl hollow spheres the peaks of Sn3d and S2p are hard to find with very small peak height. This is a direct proof that the outer layer of the hollow spheres is mainly composed by BiOCl layer.

Based on above analysis, the growth mechanism of SnS_2-incorporated BiOCl hollow spheres is illustrated in Scheme 1. In the beginning of the crystal growth, the nucleation of BiOCl and SnS_2 cystals are modulated by the absorbance and complex of PVP on the surface. PVP leads to the formation of nanoplates and the nanoplates form the flower-like structure by self-assembly which is driven by van der Waals forces and hydrogen bond among the organic molecules on the surface of nanomaterials.[27, 28] Citric acid as a biological ligand for metal ions can form strong complexes with Bi^{3+}, Al^{3+}, Ca^{2+}, Fe^{3+}, Zn^{2+}, Mg^{2+}, etc.[28] Citric acid can be hydrolyzed into $[C_6O_7H_5]^{3-}$ and H^+ which will affect the nucleation, growth and self-assembly of crystals. The $[C_6O_7H_5]^{3-}$ ions can chelate with Bi^{3+} to form $[C_6O_7H_5]^{3-}Bi^{3+}$.[14, 27] Hydrogen bond can be formed between the carboxyl of citric acid and the hydroxyl ions in $[C_6O_7H_5]^{3-}Bi^{3+}$, and between the hydroxyl ions in $[C_6O_7H_5]^{3-}Bi^{3+}$. The self-assembly growth of SnS_2-BiOCl nanoplates is controlled by the interaction between $[C_6O_7H_5]^{3-}Bi^{3+}$ and hydrogen bond. In the presence of citric acid nanoplates of BiOCl and SnS_2 are formed first. Citric acid is then absorbed on the surface of the nanoplates, with the other end forming $[C_6O_7H_5]^{3-}Bi^{3+}$ with Bi^{3+} in

the solution. The hollow structure is the result of the interaction between the $[C_6O_7H_5]^{3-}Bi^{3+}$ complex ion and hydrogen bond. The surface $[C_6O_7H_5]^{3-}Bi^{3+}$ complex ion forms BiOCl which forms the out layer of the shell of the hollow sphere.

3.4 Characterization of the photocatalytic activity of the BiOCl/SnS_2 hollow spheres

The photocatalytic activity of the BiOCl/SnS_2 hollow spheres was evaluated by the degradation of RhB, a typical organic contaminant. Fig. 7 presents the variation of RhB concentration (C/C0) as the function of irradiation time for experiments carried out under irradiation at wavelengths in the range of 385-740 nm and visible light irradiations at λ>420 nm, respectively. For comparison, the photocatalytic activity of Degussa's P25 and the degradation of RhB without photocatalysts were tested under the same conditions. The blank test without photocatalysts shows that RhB is very stable and does not decompose even after long-time illumination with UV-vis or visible light irradiations. A rapid decrease in the concentration of RhB with time is realized in the presence of the as-prepared SnS_2-incoporated BiOCl photocatalysts. For comparison, the photocatalytic property of pure SnS_2 and BiOCl were also tested. All the samples exhibited much higher photocatalytic activity under UV-vis and visible light irradiation compared to the standard (Degussa's P25). Among them the BiOCl/SnS_2 hollow spheres showed the highest RhB removal rate with total decomposition within only 50 min under UV-vis light irradiation and within only 70 min under visible light irradiation, which is a triple enhancement in comparison to the standard (Degussa's P25). After 90 minutes of visible light irradiation the degradation efficiency of RhB on pure SnS_2 and BiOCl are less than 21% and 43%, respectively, which is significantly less than that of the BiOCl/SnS_2 hollow spheres. The remarkable improvement of the photocatalytic performance of the BiOCl/SnS_2 hollow spheres is explained by three reasons. The first point is the tuning effect of SnS_2. Both the valence band and conduction band potentials of SnS_2 are more negative than those of BiOCl. This thermodynamically allows the photogenerated electron transfer from the conduction band of SnS_2 to the conduction band of BiOCl, which can enhance the separation of photogenerated electrons and holes in SnS_2 and increase the sensitization of BiOCl. Secondly the hierarchical assemble of nanoflakes greatly increases the surface area.[27, 28] Thirdly, the hierarchical architecture can allow multiple reflections of light, which enhances light-harvesting efficiency and thus increase the quantity of photogenerated electrons and holes available to participate in the photcatalytic reaction.[27, 28] It should also be pointed out that the BiOCl/SnS_2

hollow spheres show much higher activity than the flower-like structure. This is caused by at least two factors. The bigger size of the flower-like structure leads to smaller surface area and reduces the efficiency. The second is the benefit of the hollow structure: both the inner and outside wall of the sphere can be utilized in the photocatalysis, which greatly improves the efficiency. This explanation is supported by the Brunauer-Emmett-Teller (BET) specific surface areas of the SnS_2-incoporated BiOCl samples with different morphologies by using nitrogen adsorption-desorption isotherms. The BET specific surface area of SnS_2-incoporated BiOCl hollow spheres was calculated to be 32.5639 m^2g^{-1}, which was much larger than the flower-like sturcture whitout adding citric acid(23.4383 m^2g^{-1})(Fig. S5 and Table 1 in the supporting materials). The pores of the SnS_2-incoporated BiOCl hollow spheres are mesopores, which provide much better access of the solution to the reaction sites than the micropores of the flower-like structure. Besides the higher activity, the SnS_2-incoporated BiOCl hollow spheres also show strong durability during the photocatalytic degradation of RhB. After ten times of cycle test the efficiency only drops by 5%, which reaches the best durability reported in literature.[19, 28]

To further investigate the photocatalytic mechanism, the transient photocurrent responses of the samples were recorded via several irradiation on-off cycles. The representative plots are shown in Fig. 9. When the light was turned on the photocurrent reached a high point and followed by a fast decline, forming a spike, then decreased gradually until a constant value is reached. The photocurrent was instantaneously close to zero as long as the light was switched off. The initial anodic photocurrent spike is caused by the separation of electron-hole pairs at the BiOCl/SnS_2 composite[31,32]. Holes move to the BiOCl surface, where they are trapped or captured by reduced species in the electrolyte. At the same time the electrons are transported to the conduction band of SnS_2. The decay of the photocurrent is caused by the recombination of photogenerated electron-hole pairs. Instead of capturing electrons from the electrolyte, a portion of the holes at the surface of BiOCl recombine with electrons from the conduction band of SnS_2 or just accumulate at the surface[34,35]. The electrons in the conduction band of SnS_2 take part in the reduction of the photogenerated oxidized species in the electrolyte, which results in the decay of the photocurrent. When the seperation and recombination of the electron-hole pairs reach an equilibration, a constant current is reached. When the light is turned off, the holes accumulated at the BiOCl surface and the electrons in SnS_2 conduction band are

recombined simultaneously, leading to a fast drop of the photocurrent to zero. It can be seen from Fig.9 that BiOCl/SnS_2 exhibits a prompt generation of photocurrent with good reproducibility. The much higher anodic photocurrent of the BiOCl/SnS_2 composite compared with BiOCl or SnS_2 alone is a direct proof of a much higher efficiency of the separation of electron-hole pairs, which is the origin of the synergetic effect resulting in the high photocatalytic performance of the BiOCl/SnS_2 composite.

3.5 Discussion on the origin of the improved photocatalytic property of the BiOCl/SnS_2 composite

UV-vis diffuse reflectance spectroscopy of unmodified SnS_2, BiOCl and BiOCl/SnS_2 were used to study the band gap of the samples. As shown in Fig. S6, BiOCl absorbs the ultraviolet light with an absorbance edge of about 360 nm, whereas SnS_2 and BiOCl/SnS_2 exhibit an obvious red shift and show good absorptions in the visible light range with an absorbance edge around 550 and 450 nm, respectively, suggesting that the incorporation of SnS_2 can effectively extend the light absorption edge of BiOCl from ultraviolet into visible region. For the crystalline semiconductor, the band gap (E_g) can be calculated according to the following equation:

$$\alpha h\nu = A(h\nu - E_g)^{1/2}$$

where α, h, v, E_g, A are the absorption coefficient, Plank constant, light frequency, band gap energy, and a constant, respectively. Hence, E_g can be estimated by extrapolating the linear portion of $(\alpha h\nu)^2$ vs. (hv) curves (Fig. S6B). The E_g value of BiOCl, BiOCl/SnS_2 and SnS_2 are calculated to be about 3.20, 2.38, 2.17 eV, respectively. The fact that the E_g value of BiOCl/SnS_2 is between those of pure SnS_2 and BiOCl is a direct proof of the formation of the BiOCl/SnS_2 p-n junction.

The photoelectrochemical method is used to determine the conduction band (CB) of SnS_2 and valence band (VB) of BiOCl semiconductors. The photocurrent spectra of SnS_2 and BiOCl are shown in Fig. S7 a and b. In the photocurrent spectra of SnS_2, the flat band potential is at -0.98 V versus SCE. For n-type semiconductor, the flat band potential is closely related to the bottom of the CB. The VB of SnS_2 is calculated to be 1.19 V according to the corresponding E_g value (2.17 eV). The photocurrent onset potential (conduction band edge) of BiOCl is at +0.88 V versus SCE. As the band gap energy of BiOCl is 3.20 eV, the CB edge is calculated to be -2.32 V. The energy band

structure diagram of SnS_2 and BiOCl is schematically represented in Fig. S8. BiOCl is a p-type semiconductor with Fermi level close to the VB, whereas SnS_2 is a n-type semiconductor with Fermi level close to CB. When the Fermi levels of p-BiOCl and n-SnS_2 reach equilibration, an internal electric field directed from n-SnS_2 to p-BiOCl is built, preventing the charge migrating from n-SnS_2 into p-BiOCl. The energy band positions of BiOCl in BiOCl/SnS_2 heterojunction shift upward along the Fermi level ($E_{f,n}$) and those of SnS_2 shift downward along its Fermi level ($E_{f,p}$). [36] As a result, the band positions of BiOCl and SnS_2 in the heterojunction have a type-II band structure in which the CB and VB of SnS_2 lie below those of BiOCl. [37] The formation of heterojunction between BiOCl and SnS_2 results in a pseudo band (PB in Fig.S8) between VB and CB of BiOCl, which can accept photogenerated electrons from VB. Thus the band gap of BiOCl is narrowed, leading to response to visible light. The electrons in the PB can continue to move to the CB of BiOCl when absorbing more visible light. Due to the effect of internal electric field, the photoelectrons on the CB bottom of BiOCl will transfer to that of SnS_2 and be trapped by oxygen (O_2) to form reactive super oxide radicals ($O_2^{\cdot-}$) or $OH^{\cdot}$, and the holes remained in the VB of BiOCl will react with the reactants adsorbed on the surface of BiOCl/SnS_2. Thus, the photogenerated electron-hole pairs will be effectively separated because of the formation of p-n junction formed between BiOCl and SnS_2, resulting in a reduced electron-hole recombination rate.

4. Conclusions

In summary, a novel BiOCl/SnS_2 hollow spheres is synthesized for the first time by a facile one-pot hydrothermal process. A triple enhancement in the visible light photocatalytic performance of the hollow spheres is observed, which is explained by the hierarchical structure and the doping effect of SnS_2 to BiOCl. The easy synthesis and high efficiency makes the novel composite a very promising candidate for

application in photocatalysis. The idea of this work can also be used to tune electronic and band structure of other wide-band-gap semiconductors for application in both solar energy conversion and photocatalysis in environmental protection.

Acknowledgements:

This work was supported by National Natural Science Foundation of China (21276104, 21106190, 21476096), Pearl River S&T Nova Program of Guangzhou (2013J2200040), the Fundamental Research Funds for the Central Universities.

References

[1] Maeda, K.; Teramura, K.; Lu, D.; Takata, T.; Saito, N.; Inoue Y.; Domen, K. Photocatalyst releasing hydrogen from water Nature 2006, 440, 295-295.

[2] Khan, S. U. M.; Al-Shahry, M.; Ingler Jr, W. B. Efficient Photochemical Water Splitting by a Chemically Modified n-TiO2 Science 2002, 297, 2243-2245.

[3] Mukherji, A.; Marschall, R.; Tanksale, A.; Sun, C.; Smith, S. C.; Lu, G. Q.; Wang, L. N-Doped CsTaWO6 as a New Photocatalyst for Hydrogen Production from Water Splitting Under Solar Irradiation Adv. Funct. Mater. 2011, 21, 126-132.

[4] Maeda, K.; Xiong, A.; Yoshinaga, T.; Ikeda, T.; Sakamoto, N.; Hisatomi, T.; Takashima, M.; Lu, D.; Kanehara, M.; Setoyama, T. Photocatalytic overall water splitting promoted by two different cocatalysts for hydrogen and oxygen evolution under visible light Angew. Chem. 2010, 122, 4190-4193.

[5] Pan, C.; Xu, J.; Wang, Y.; Li, D.; Zhu, Y. Dramatic Activity of C3N4/BiPO4 Photocatalyst with Core/Shell Structure Formed by Self-Assembl. Adv. Funct. Mater. 2012, 22 , 1518-1524.

[6] Zhou, W.; Yin, Z.; Du, Y.; Huang, X.; Zeng, Z.; Fan, Z.; Liu, H.; Wang, J.; Zhang, H. Synthesis of few-layer MoS2 nanosheet-coated TiO2 nanobelt heterostructures for enhanced photocatalytic activities Small 2013, 9, 140-147.

[7] Etacheri, V.; Seery, M. K.; Hinder, S. J.; Pillai, S. C. Oxygen Rich Titania: A Dopant Free, High Temperature Stable, and Visible-Light Active Anatase Photocatalyst Adv. Funct. Mater. 2011, 21, 3744-3752.

[8] Qiu, X.; Miyauchi, M.; Yu, H.; Irie, H.; Hashimoto, K. Visible-Light-Driven Cu(II)-(Sr1-yNay)(Ti1-xMox)O-3 Photocatalysts Based on Conduction Band Control and Surface Ion Modification J. Am. Chem. Soc. 2010, 132, 15259-15267.

[9] Chakraborty, A. K.; Rawal, S. B.; Han, S. Y.; Chai, S. Y.; Lee, W. I. Enhancement of visible-light photocatalytic efficiency of BiOCl/Bi2O3 by surface modification with WO3 Appl. Catal. A 2011, 407, 217-223.

[10] Asahi, R.; Morikawa, T.; Ohwaki, T.; Aoki, K.; Taga, Y. Visible-light photocatalysis in nitrogen-doped titanium oxides Science 2001, 293, 269-271.

[11] Sato, S.; Asahi, R.; Morikawa, T.; Ohwaki, T.; Aoki, K.; Taga, Y. Photocatalysts sensitive to visible light Science 2002, 295, 626-627.

[12] Sakthivel, S.; Kisch, H. Daylight photocatalysis by carbon-modified titanium dioxide Angew. Chem. Int. Ed. 2003, 42 , 4908-4911.

[13] Chen, X.; Liu, L.; Yu, P. Y.; Mao, S. S. Increasing solar absorption for photocatalysis with black hydrogenated titanium dioxide nanocrystals Science 2011, 331, 746-750.
[14] Zhao, K.; Zhang, L.; Wang, J.; Li, Q.; He, W.; Yin, J. J. Surface Structure-Dependent Molecular Oxygen Activation of BiOCl Single-Crystalline Nanosheets J. Am. Chem. Soc. 2013, 135, 15750-15753.
[15] Guan, M.; Xiao, C.; Zhang, J.; Fan, S.; An, R.; Cheng, Q.; Xie, J.; Zhou, M.; Ye, B.; Xie, Y. Vacancy associates promoting solar-driven photocatalytic activity of ultrathin bismuth oxychloride nanosheets J. Am. Chem. Soc. 2013, 135, 10411-10417.
[16] Gnayem, H.; Sasson, Y. Hierarchical Nanostructured 3D Flowerlike BiOClxBr1−xSemiconductors with Exceptional Visible Light Photocatalytic Activity ACS Catal. 2013, 3, 186-191.
[17] Jiang, J.; Zhang, L.; Li, H.; He, W.; Yin, J. J. Self-doping and surface plasmon modification induced visible light photocatalysis of BiOCl Nanoscale 2013, 5, 10573-10581.
[18] Dong, F.; Sun, Y.; Fu, M.; Wu, Z.; Lee, S. C. Room temperature synthesis and highly enhanced visible light photocatalytic activity of porous BiOI/BiOCl composites nanoplates microflowers J. Hazard. Mater. 2012, 219, 26-34.
[19] Zhang, K.; Zhang, D.; Liu, J.; Ren, K.; Luo, H.; Peng, Y.; Li, G.; Yu, X. A novel nanoreactor framework of iodine-incorporated BiOCl core–shell structure: enhanced light-harvesting system for photocatalysis CrystEngComm 2012, 14, 700-706.
[20] Mu, Q.; Zhang, Q.; Wang, H.; Li, Y. Facile growth of vertically aligned BiOCl nanosheet arrays on conductive glass substrate with high photocatalytic properties J. Mater. Chem. 2012, 22, 16851-16857.
[21] Gou, X. L.; Chen, J.; Shen, P. W. Synthesis, characterization and application of SnSx (x=1, 2) nanoparticles Mater. Chem. Phys. 2005, 93, 557-566.
[22] Cheng, H.; Huang, B.; Dai, Y.; Qin, X.; Zhang, X. One-step synthesis of the nanostructured AgI/BiOI composites with highly enhanced visible-light photocatalytic performances Langmuir, 2010, 26 , 6618-6624.
[23] Zhang, X.; Zhang, L.; Xie, T.; Wang, D. Low-Temperature Synthesis and High Visible-Light-Induced Photocatalytic Activity of BiOI/TiO2 Heterostructures J. Phys. Chem. C 2009, 113, 7371-7378.
[24] Yang, F.; Han, G.; Fu, D.; Chang, Y.; Wang, H. Improved photodegradation activity of TiO2 via decoration with SnS2 nanoparticles Mater. Chem. Phys. 2013, 140, 398-404.
[25] Lei, Y.; Song, S.; Fan, W.; Xing,Y.; Zhang, H. Facile Synthesis and Assemblies of Flowerlike SnS2 and In3+-Doped SnS2: Hierarchical Structures and Their Enhanced Photocatalytic Property J. Phys. Chem. C 2009, 113, 1280-1285.
[26] Reddy, K. H.; Martha, S.; Parida, K. M. Fabrication of novel p-BiOI/n-ZnTiO3 heterojunction for degradation of rhodamine 6G under visible light irradiation Inorg. Chem. 2013, 52, 6390-6401.
[27] Peng, S.; Li, L.; Zhu, P.; Wu, Y.; Srinivasan, M.; Mhaisalkar, S. G.; Ramakrishna, S.; Yan, Q. Controlled synthesis of BiOCl hierarchical self-assemblies with highly efficient photocatalytic properties Asian. J. Chem. 2013, 8 , 258-268.
[28] Zhang, K.; Liang, J.; Wang, S.; Liu, J.; Ren, K.; Zheng, X.; Luo, H.; Peng, Y.; Zou, X.; Bo, X.; Li, J.; Yu, X. BiOCl Sub-Microcrystals Induced by Citric Acid and Their High Photocatalytic Activities Cryst. Growth Des. 2012, 12, 793-803.

[29] Gong, X.; Bao, Y.; Qiu, C.; Jiang, C. Individual nanostructured materials: fabrication and surface-enhanced Raman scattering Chem. Comm. 2012, 48, 7003-7018.
[30] Zhang, L.; Gong, X.; Bao, Y.; Zhao, Y.; Xi, M.; Jiang, C. Electrospun nanofibrous membranes surface-decorated with silver nanoparticles as flexible and active/sensitive substrates for surface-enhanced Raman scattering Langmuir 2012, 28, 14433-14440.
[31] Gong, X.; Han, L.; Yue, Y.; Gao, J.; Gao, C. Influence of assembly pH on compression and Ag nanoparticle synthesis of polyelectrolyte multilayers J. Colloid Interface Sci. 2011, 355, 368-373.
[32] Osterloh, F. E. Inorganic materials as catalysts for photochemical splitting of water Chem. Mater. 2007, 20, 35-54.
[33] Henning, A. M.; Watt, J.; Miedziak, P. J.; Cheong, S.; Santonastaso, M.; Song, M.; Takeda,Y.; Kirkland, A. I.; Taylor, S. H.; Tilley, R. D. Gold-Palladium Core-Shell Nanocrystals with Size and Shape Control Optimized for Catalytic Performance Angew. Chem. Int. Ed. 2013, 52, 1477-1480.
[34] Yu, J.; Dai, G.; Huang, B. Fabrication and Characterization of Visible-Light-Driven Plasmonic Photocatalyst Ag/AgCl/TiO2 Nanotube Arrays J. Phys. Chem. C 2009, 113, 16394-16401.
[35] Dai, G.; Yu, J.; Liu, G. Synthesis and Enhanced Visible-Light Photoelectrocatalytic Activity of p−n Junction BiOI/TiO2 anotube Arrays J. Phys. Chem. C 2011, 115, 7339-7346.
[36] Zhao, W.; Wang, Y.; Yang, Y.; Tang, J.; Yang, Y. N. Carbon spheres supported visible-light-driven CuO-BiVO4 heterojunction: preparation, characterization, and photocatalytic properties, Appl. Catal. B: Environ. 2012, 115, 90–99.
[37] Wang, Y. J.; Wang, Q. S.; Zhan, X. Y.; Wang, F. M.; Safdar, M.; He, J. Visible light driven type II heterostructures and their enhanced photocatalysis properties: a review, Nanoscale, 2013, 5 8326–8339.

Figures and caption:

Fig. 1 FESEM images of as prepared SnS_2-incorporated BiOCl flower-like structure without citric acid (a, b) and hollow spheres with citric acid (c, d).

Fig. 2 XRD patterns of (a) pure SnS_2, (b) pure BiOCl, (c) SnS_2-incorporated BiOCl flower-like structure without citric acid and (d) SnS_2-incorporated BiOCl hollow spheres with citric acid.

Fig. 3 FETEM images (a, b and c) and SEAD pattern (d) of as prepared SnS_2-incorporated BiOCl HMSs. microspheres.

Fig. 4 Onsite growth of crystal by electron beam bombardment, (a): selected flake before bombardment, (b and c): after bombardment, (d): HRTEM of the bombarded area.

Fig. 5 EDS mapping of SnS_2-incorparated BiOCl hollow sphere, the elements presented are (a), Bi (b), O (c), Cl (d), Sn (e), S (f).

Fig. 6 XPS spectra of BiOCl, SnS_2 and SnS_2-incorporated BiOCl hollow spheres, survey spectrum (a), Bi 4f (b), O 1s (c), Cl 2p (d), Sn 3d (e), S 2p (f).

Scheme 1. Proposed formation mechanism of SnS_2-incorporated BiOCl hierarchical nanostructures.

Fig. 7 Comparison of visible-light photocatalytic activities, (a) SnS_2-incoporated BiOCl hollow spheres, (b) SnS_2-incoporated BiOCl hollow spheres of flower-like structure, (c) pure SnS_2, (d) pure BiOCl, (e) P_{25}, (f) adsorption in dark, (g) degradation of 10 mg L^{-1} RhB without photocatalyst underUV-vis (385-740 nm) (A) and visible light (λ>420 nm) irradiations (B).

Fig. 8 Cycling degradation curves of SnS_2-incoporated BiOCl hollow spheres on the degradation of 10 mg L^{-1} RhB under visible light (λ>420 nm) irradiations.

Fig.9 Comparison of transient photocurrent response of pure SnS_2, pure BiOCl and BiOCl/SnS_2 in 0.1 M Na_2SO_4 aqueous solution under visible-light irradiation vs SCE.

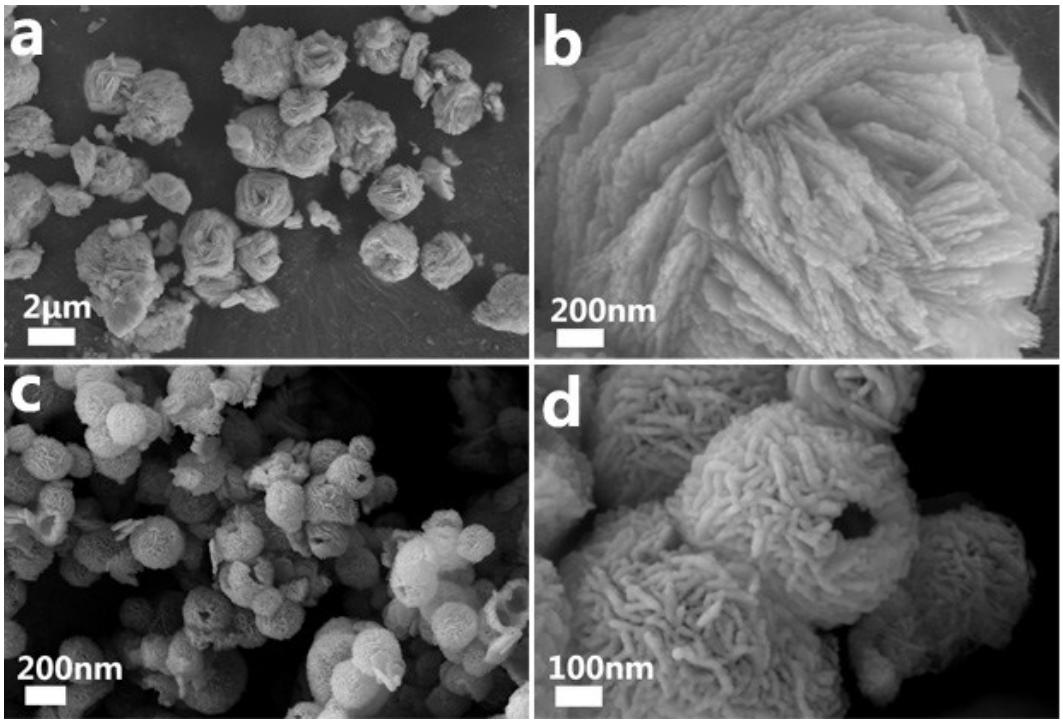

Fig. 1 FESEM images of as prepared SnS_2-incorporated BiOCl flower-like structure without citric acid (a, b) and hollow spheres with citric acid (c, d).

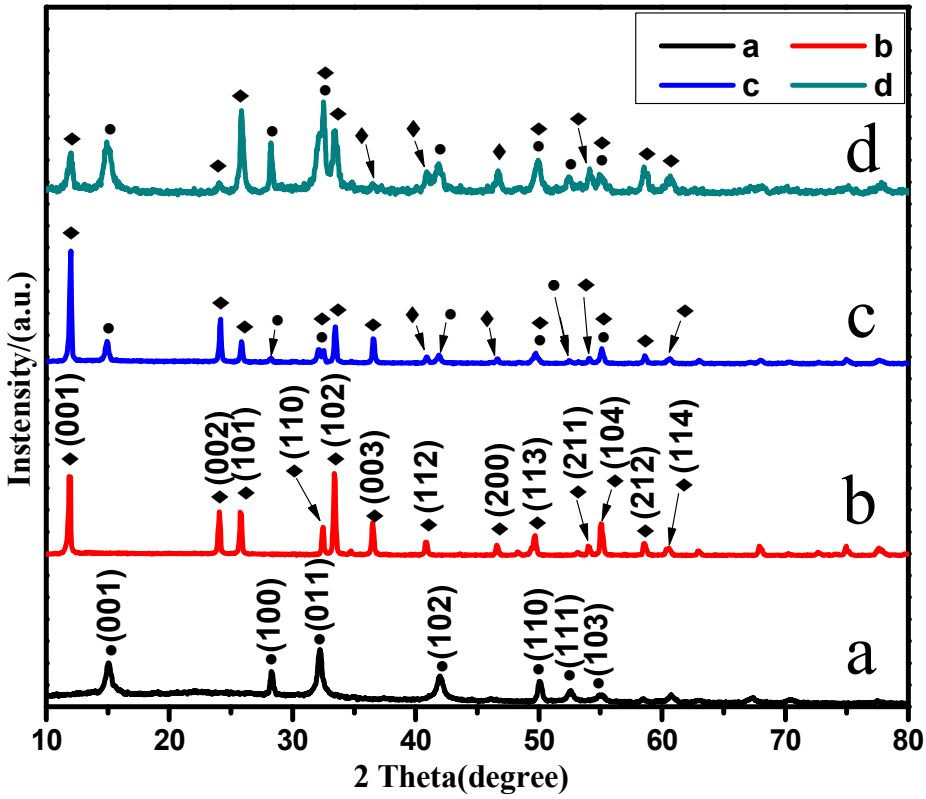

Fig. 2 XRD patterns of (a) pure SnS_2, (b) pure BiOCl, (c) SnS_2-incorporated BiOCl flower-like structure without citric acid and (d) SnS_2-incorporated BiOCl hollow spheres with citric acid.

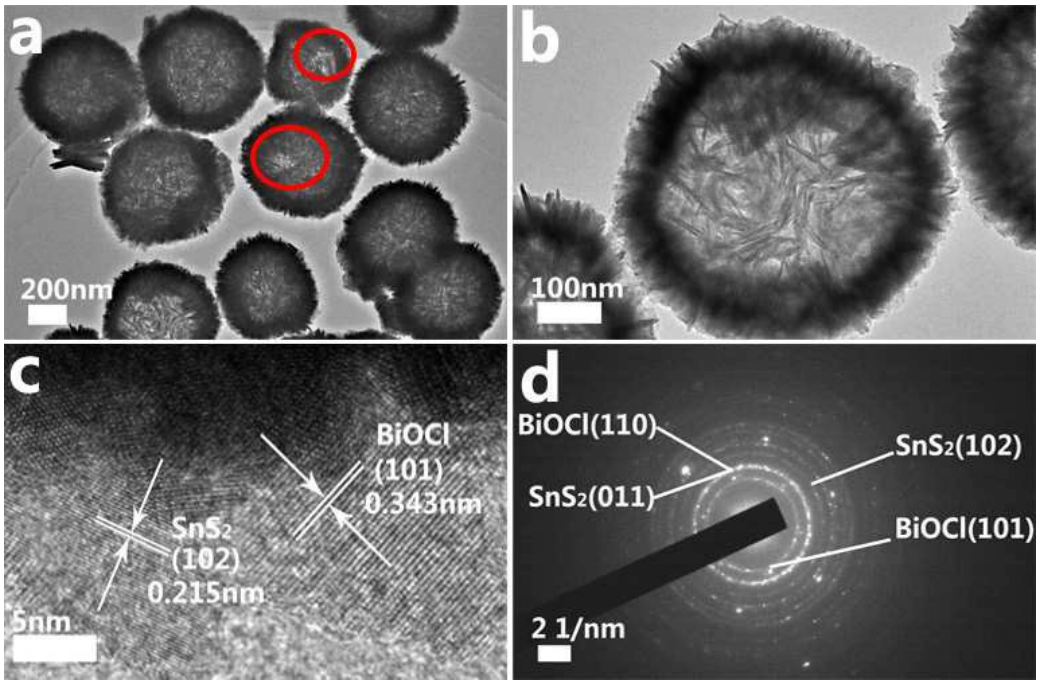

Fig. 3 FETEM images (a, b and c) and SEAD pattern (d) of as prepared SnS_2-incorporated BiOCl HMSs. microspheres.

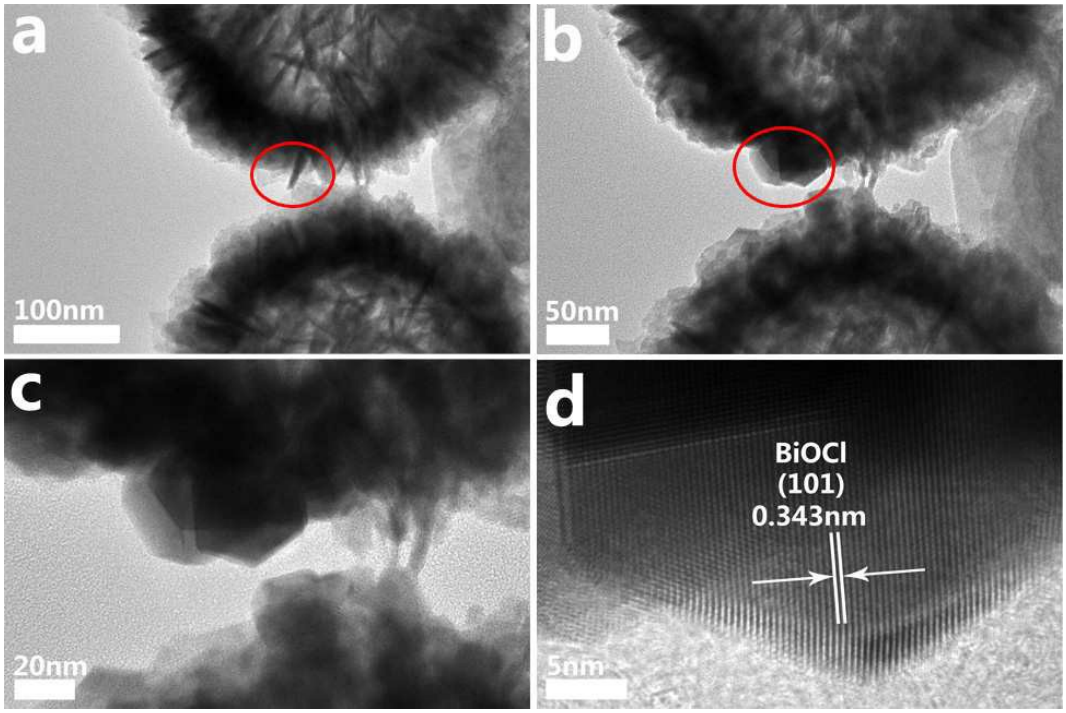

Fig. 4 Onsite growth of crystal by electron beam bombardment, (a): selected flake before bombardment, (b and c): after bombardment, (d): HRTEM of the bombarded area.

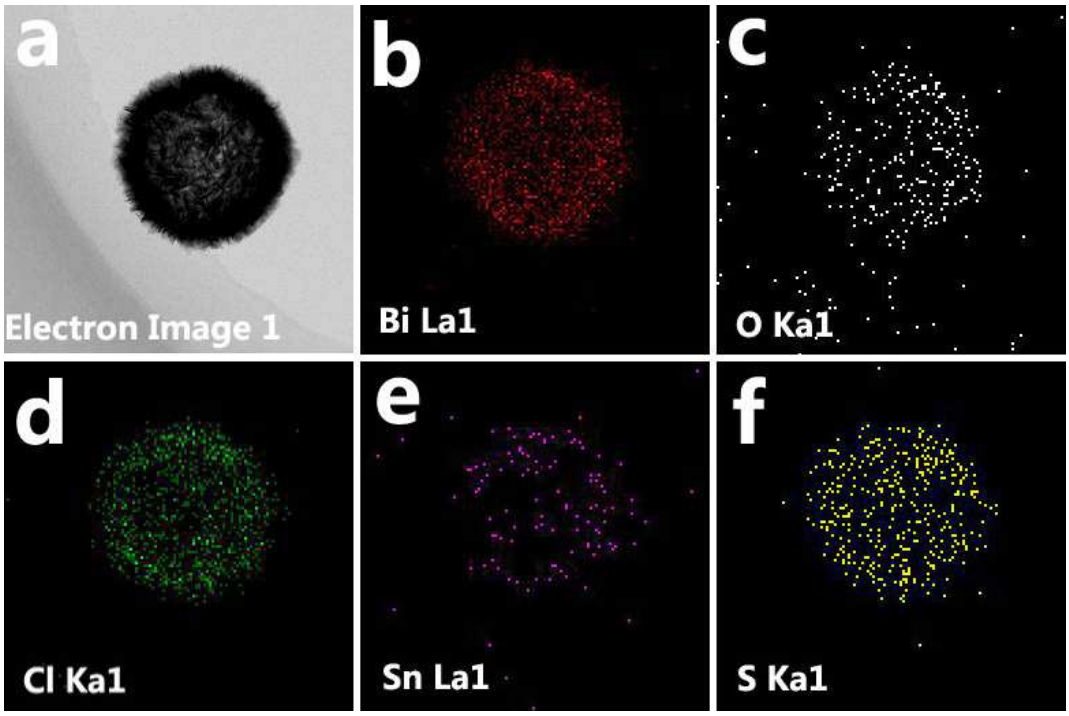

Fig. 5 EDS mapping of SnS_2-incorparated BiOCl hollow sphere, the elements presented are (a), Bi (b), O (c), Cl (d), Sn (e), S (f).

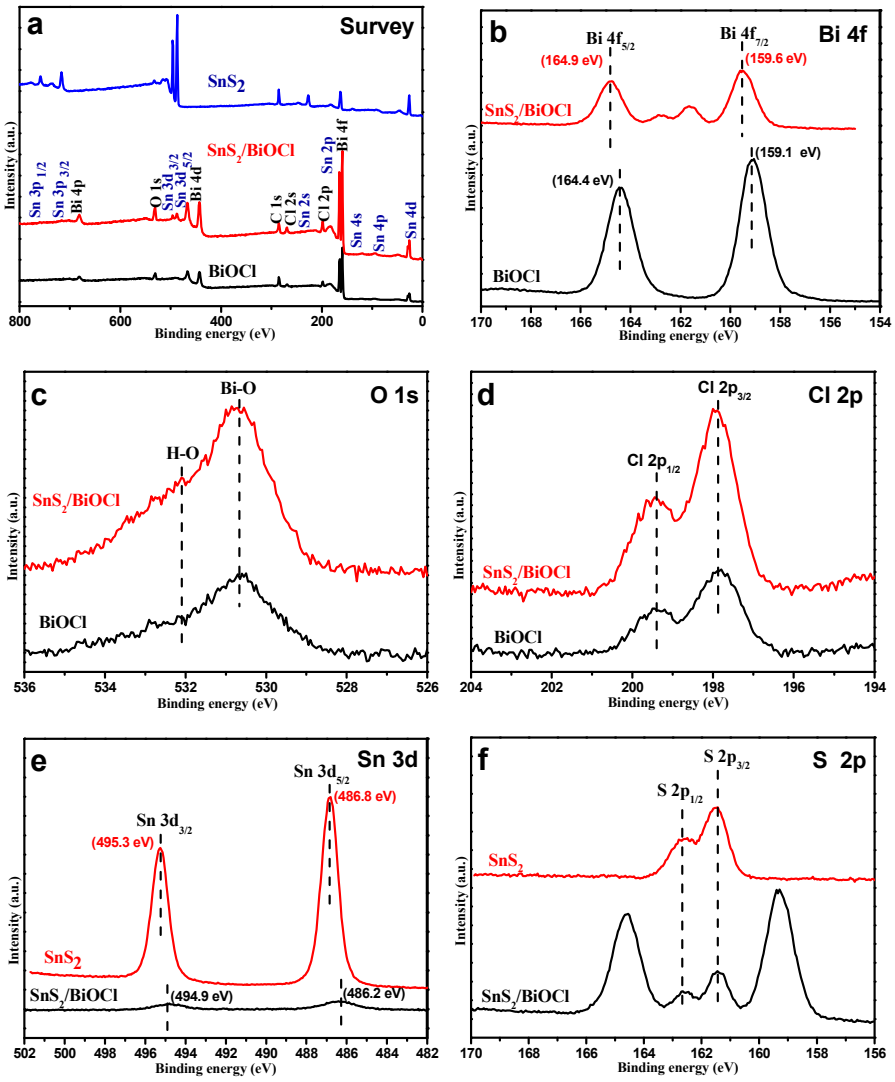

Fig. 6 XPS spectra of BiOCl, SnS_2 and SnS_2-incorporated BiOCl hollow spheres, survey spectrum (a), Bi 4f (b), O 1s (c), Cl 2p (d), Sn 3d (e), S 2p (f).

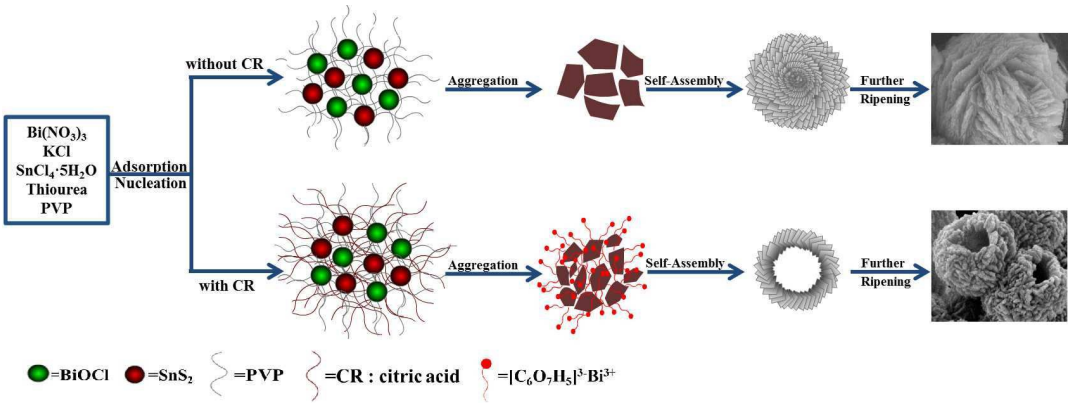

Scheme 1. Proposed formation mechanism of SnS_2-incorporated BiOCl hierarchical nanostructures.

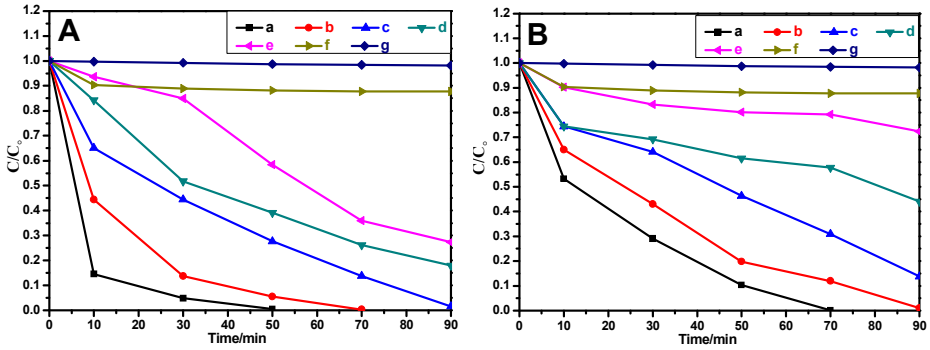

Fig. 7 Comparison of visible-light photocatalytic activities, (a) SnS_2-incoporated BiOCl hollow spheres, (b) SnS_2-incoporated BiOCl hollow spheres of flower-like structure, (c) pure SnS_2, (d) pure BiOCl, (e) P_{25}, (f) adsorption in dark, (g) degradation of 10 mg L^{-1} RhB without photocatalyst under UV-vis (385-740 nm) (A) and visible light (λ>420 nm) irradiations (B).

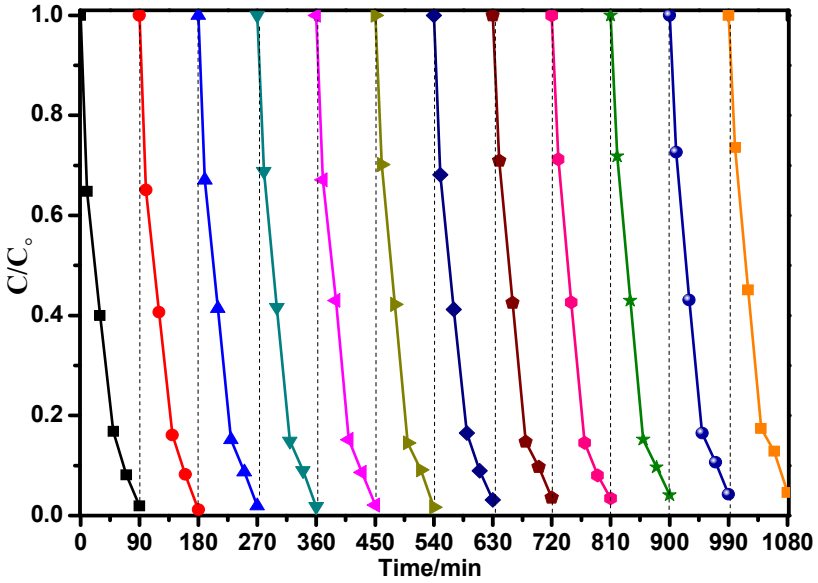

Fig. 8 Cycling degradation curves of SnS_2-incoporated BiOCl hollow spheres on the degradation of 10 mg L^{-1} RhB under visible light (λ>420 nm) irradiations.

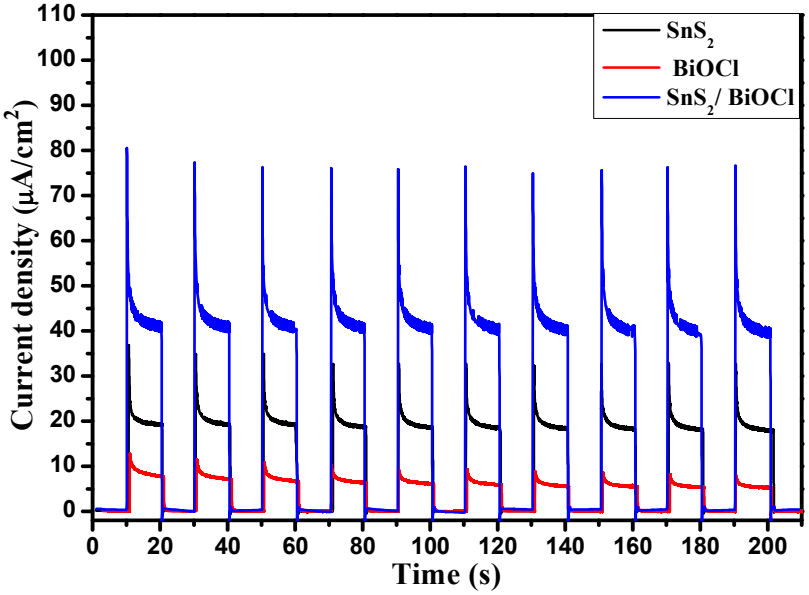

Fig.9 Comparison of transient photocurrent response of pure SnS_2, pure BiOCl and BiOCl/SnS_2 in 0.1 M Na_2SO_4 aqueous solution under visible-light irradiation vs SCE.

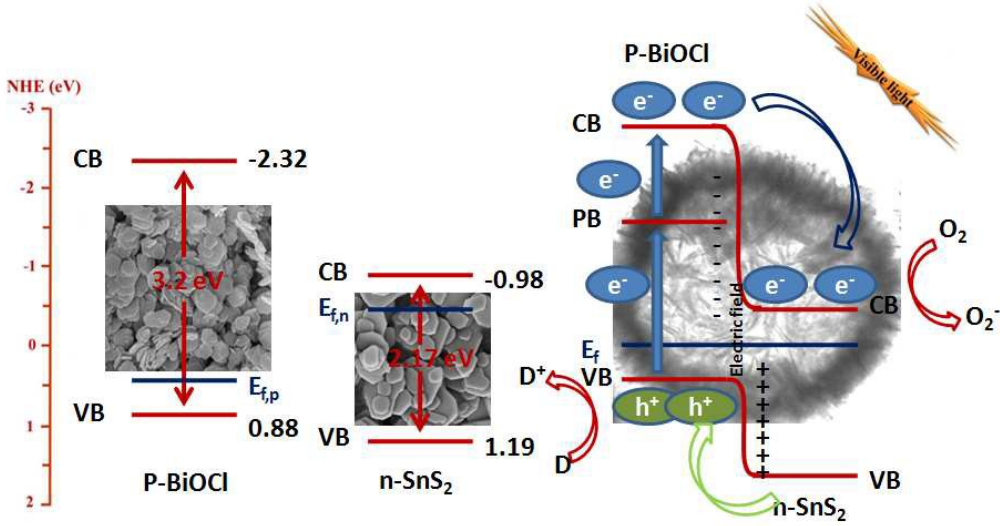

A kind of novel SnS_2-incorporated BiOCl hollow spheres are synthesized. The band structure tuning effect and the morphological benefits of the hollow sphere structure with great improved performance in photocatalysis.